Supplementary Information for

Exceptional-point-enhanced phase sensing

Wenbo Mao, Zhoutian Fu, Yihang Li, Lan Yang*

Department of Electrical and Systems Engineering, Washington University, St Louis, MO, 63130, USA.

* Correspondence to: yang@seas.wustl.edu

Supplementary Section 1: Theoretical analysis of splitting

In the Methods section, we have solved the eigenvalues of the two-mode-coupled system as

$$\sigma_{\pm} \equiv \Omega \mp i\,\Gamma/2 = \pm\sqrt{\tilde{A}(\tilde{A}+\tilde{\mu})} \tag{S1}$$

in which $\tilde{A}$ is the complex bidirectional coupling strength and $\tilde{\mu}$ is the complex unidirectional coupling strength (see Fig. 1 in the main text). The spectral characteristics, frequency splitting and linewidth difference, are defined as $2|\Omega|/2\pi$ and $2|\Gamma|/2\pi$, respectively. We plot them in Supplementary Figure 1 at the coupling strengths μ/A = 0.5, 1.0, and 1.5, varying the phase $\Delta\varphi$. The coalescence of eigenstates at the EP results in both frequency splitting and linewidth difference reaching zero simultaneously. As perturbed by a small phase $\Delta\varphi$, the change of splitting around the EP state ($\mu/A = 1$) is much larger than that at other states, showing EP-enhanced phase sensing. Note that a more remarkable EP enhancement is observed as perturbed by smaller phase changes (Supplementary Figure 2), while the superiority of EPs degrades for larger perturbations, for example, $\Delta\varphi$ = 1.

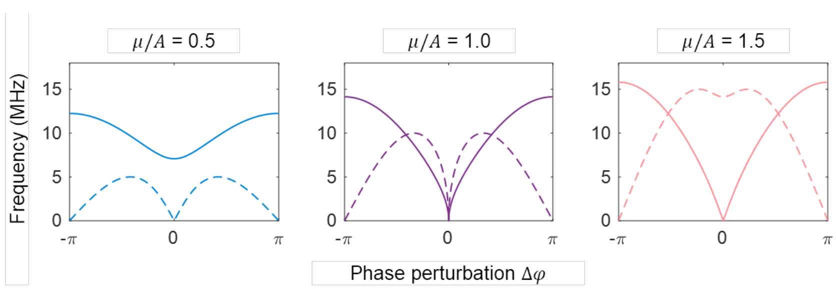

Supplementary Figure 1 | Frequency splitting (solid lines) and linewidth difference (dashed lines) at different coupling strengths. The splitting exhibits more drastic change around the EP ($\mu/A = 1$). Parameters: $A/2\pi = 5$ MHz, $\alpha = 0$, $\varphi_0 = \pi$.

The symmetry of the splitting curves is affected by the parameter α (Supplementary Figure 3). When the bidirectional coupling strength $\tilde{A}$ is purely real, i.e., α = 0, the curves are symmetric about the y-axis ($\Delta\varphi$ = 0). However, the dissipative term of the coupling cannot be avoided since the scatterer also acts as a loss channel, leading to non-zero α. Our experimental results (Figure 3) display the slight asymmetry of the fitted curves. We have derived the splitting with $\Delta\varphi \ll 1$ in the Methods section, $\sigma_{\pm} \approx \pm A e^{i(\alpha-\pi/4)}\sqrt{\Delta\varphi}$. Assuming $\Delta\varphi > 0$, the frequency splitting, i.e., the real part of $\sigma_{\pm}$, is given as

$$2\left|\mathrm{Re}(\sigma_{\pm})\right| \approx 2A\left|\cos\left(\alpha - \frac{\pi}{4}\right)\right|\sqrt{\Delta\varphi} \tag{S2}$$

Theoretically, the maximum response to a small phase perturbation occurs at $\alpha = \pi/4$. The EP enhancement can be further improved $|\cos(0)|/|\cos(-\pi/4)| = \sqrt{2} \approx 1.4$ times than the current results. One may tune the α by a chromium-coated nanotip[1].

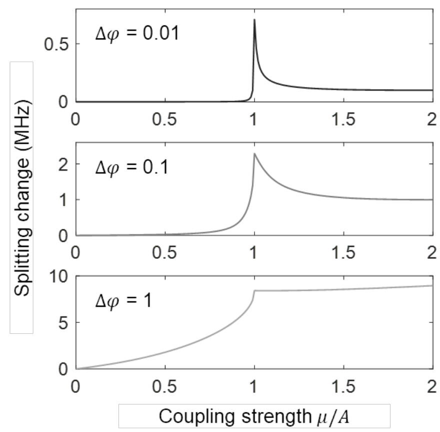

Supplementary Figure 2 | Change of splitting with a phase perturbation. The EP-enhancement is more significant for a smaller perturbation $\Delta\varphi$. With a larger $\Delta\varphi$ applied, the enhancement degrades since the changes of splitting at $\mu/A > 1$ could be larger than that at $\mu/A = 1$ (EP).

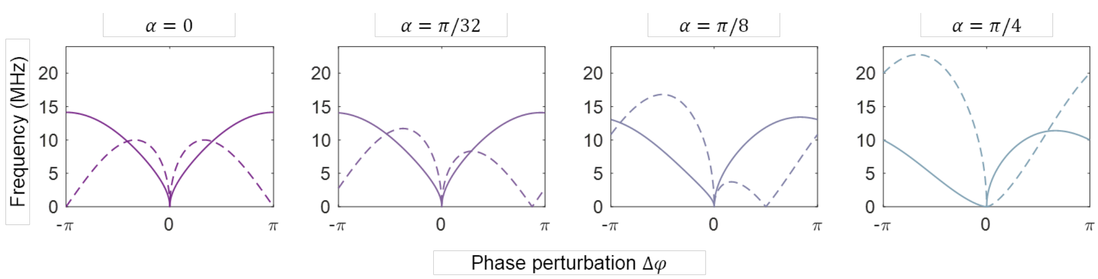

Supplementary Figure 3 | Changes of the frequency splitting (solid lines) and linewidth difference (dashed lines) as the parameter α varies. The curves are symmetric about the y-axis in the case of $\alpha = 0$. With α increasing, the curves become asymmetric, and the change of frequency splitting at a sufficiently small phase perturbation ($0 < \Delta\varphi \ll 1$) also increases until reaching the maximum at $\alpha = \pi/4$. Parameters: $\mu = A = 2\pi \times 5$ MHz, $\varphi_0 = \pi + \alpha$.

Supplementary Section 2: Reflection-type remote strain sensor

As described in the main text, the reflection-type sensor (RS) is constructed by the fiber stretched by a piezo (PZ) stage and a fiber-based mirror (FBM). The length of stretched fiber l is set as 8 cm. The movement of the PZ stage, driven by an arbitrary waveform generator and an amplifier, leads to the fiber strain and the optical phase change. The phase change is accumulated twice due to the reflection of the FBM. To avoid unwanted mechanical instability, all the components are fixed inside an acrylic box that is placed on a suspending optical table.

Compared with our EP setup, the RS is characterized by a Mach-Zehnder interferometer (MZI). The input power is the same as the probe power (2.5 μW) of the EP sensing experiment. An optical circulator helps to connect the RS to one arm (Supplementary Figure 4b). The output voltages of the photodetector (PD) are recorded as the strain varies in Supplementary Figure 4c. The shading area represents the electric noise 2.45 mV through a 20-MHz low-pass filter. The detection limit is derived as 57 nε.

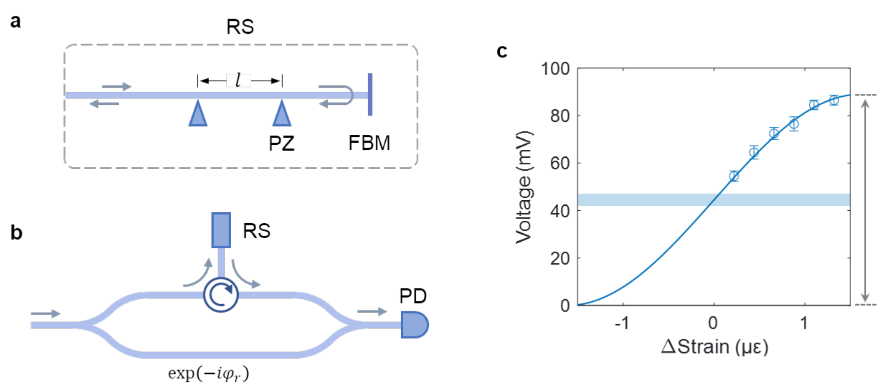

Supplementary Figure 4 | Characterization of the reflection-type non-resonant strain sensor by an MZI. a, Schematic of the RS for strain sensing. **b**, Characterization of the RS by an MZI. The RS is connected to one arm by an optical circulator. **c**, Measured signals as the applied strain increases when the reference phase φ_r is locked at $\pi/2$. The measurable range of the strain is marked by the arrow. RS, reflection-type sensor; PZ, piezo; FBM, fiber-based mirror; PD, photodetector.

The transmission spectra of the EP sensing system are shown in Supplementary Figure 5, as perturbed by a pulsed strain, with the period 2 s, the duty cycle 50%, and the amplitude 1.32 με. The driving voltage is applied to the PZ stage for the generation of the fiber strain. By reducing the splitting fluctuation caused by mechanical instability, such as replacing the fragile tapered fibers with on-chip waveguides, the EP sensing system can achieve a better detection limit.

The advantage of EP states, i.e., higher sensitivity, lies in their susceptibility to small phase change. In the main text, Figure 4c shows that the frequency splitting at an EP is larger than that in the case of $\mu > A$, with the strain perturbation 0.16 με. For the larger perturbation, for example 0.33 με, the magnitude of splitting at the EP ($\mu = A$) is very close to that at the non-EP ($\mu > A$) (Supplementary Figure 6).

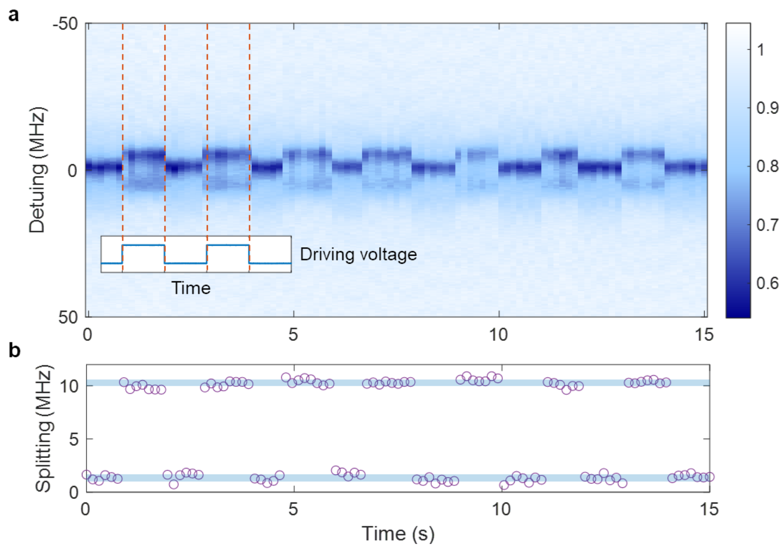

Supplementary Figure 5 | Transmission spectra and fitted frequency splitting. The system at an EP state is perturbed by a 2s 50% pulsed strain of the fiber (1.32 με). The fluctuations of the frequency splitting at two states are 0.32 MHz and 0.31 MHz, respectively.

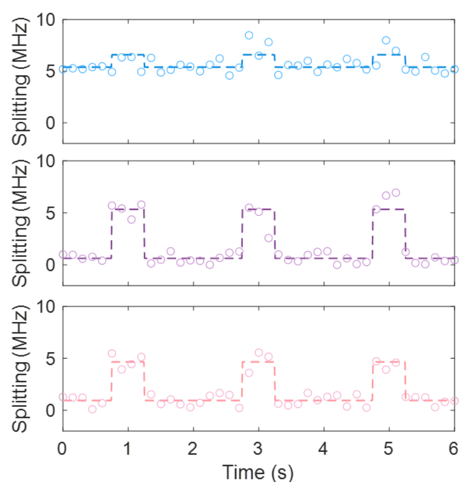

Supplementary Figure 6 | Frequency splitting in response to a stronger pulsed strain. The amplitude of strains is 0.33 με. From top to bottom, the system is at the states $\mu < A$, $\mu = A$ (EP), and $\mu > A$, respectively. The EP enhancement is negligible for large perturbations.

Supplementary Section 3: Transmission-type remote strain sensor

The transmission-type sensor (TS) is based on a fiber ring resonator, constructed from a 1:1 fiber splitter with the two interlinked ports externally connected. The theoretical expressions can be derived from the matrix method[2]

$$b_1 = \frac{-s + te^{-i\theta}}{-st + e^{-i\theta}} \tag{S3}$$

$$\text{Transmission} = |b_1|^2,\ \text{Phase} = \arg(b_1)$$

where t is the amplitude ratio of the beam splitter, s is the inner circulator factor, $\theta = \omega L/c$ represents the phase accumulation per circle, and L is the length of the fiber resonator. In our experiments, the fiber ring resonator works in the over-coupling regime to reduce the transmission variation with changing detuning[3]. The transmission of the TS affects the unidirectional coupling strength μ, a critical parameter for EP tuning. The approach to introducing the fiber strain is the same as described in Supplementary Section 2.

The TS is characterized by an MZI, which consists of three fiber splitters and one fiber combiner (Supplementary Figure 7b). The transmission and the phase response of the TS are monitored by PD1 and PD2, respectively, while PD3 is used to check the reference beam. Supplementary Figure 7c displays the measured transmission and the phase change. The curve fitting gives t = 0.67, s = 0.98, and L = 0.56 m. The phase change is obtained from the interference pattern. The maximum slope is about 4 times larger than the phase change without the resonant structure (dashed line). The interference patterns (Supplementary Figure 7d) vary with different phases of the reference beam ($-\varphi_r$). The detection limit (25 nε) is derived from the noise level and estimated at the maximum slope at $\varphi_r \approx \pi/2$.

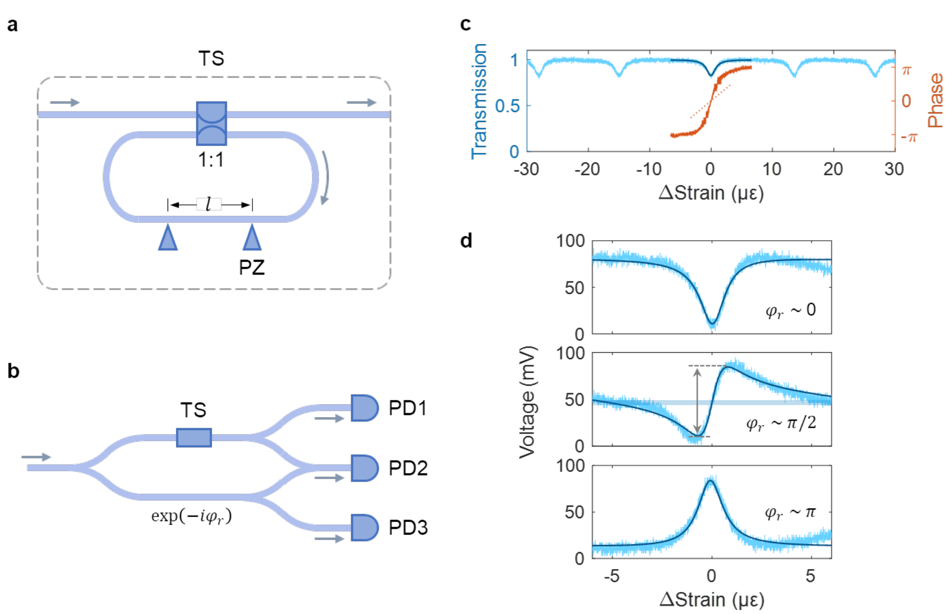

Supplementary Figure 7 | Characterization of the transmission-type resonant strain sensor using an MZI. a, Schematic of the fiber ring resonator for strain sensing. **b**, Characterization of the TS using an MZI. The transmission (PD1) and phase (PD2) of the light through the TS, along with the transmission of the reference path (PD3), are monitored. **c**, The measured transmission and phase change of the TS. Dashed line: the phase change without the resonant structure. **d**, Signal output of PD2. Fitted φ_r/π = 0.04, 0.48, 0.98, respectively. The measurable range of the strain is marked by the arrow. TS, transmission-type sensor; PZ, piezo; PD, photodetector.

Supplementary Section 4: EP enhancement of detection limit

In the main text, we have demonstrated the improvement of the detection limit by operating a sensor at EP states. The theoretical analysis reveals that the frequency splitting around a second-order EP scales as $\sqrt{\epsilon}$ and the enhancement factor $1/\sqrt{\epsilon}$ tends to infinity for a small perturbation $\epsilon \to 0$. However, the EP-enhanced fiber strain sensing demonstrates a finite improvement in the detection limit. The detection limit of this EP platform is determined by the fluctuation of splitting, as quantified by SNR = 1. The fluctuation origins from both the optical system and the electric measurement components.

(1) Mechanical instability that deviates the system from an EP state. Examples include airflow and the vibration of the optical table affecting the gap between the tapered fibers and the microtoroid (μ), as well as the unwanted phase change in the unfixed fiber that connects the control and sensing unit (φ_0). Uncompensated thermal drifting of the piezo components in the translation stages or the phase shifter is also a source of mechanical instability.

(2) Thermorefractive noise in the high-quality-factor (Q) microresonator, which can be suppressed by reducing the optical power and using a medium with a compensated thermo-optic coefficient.

(3) Drift in the tunable laser output, such as variations in optical power and center wavelength. The slowly drifted system can be maintained at EPs by ensuring the reflection is zero.

(4) Electric noise of the photodetector and the oscilloscope, particularly noticeable in the case of weak optical probe signals (several microwatts to nanowatts level), which can be mitigated by improving the photodetector responsivity and applying a low-pass filter to electrical signals.

In our experiments, the splitting fluctuation is dominated by mechanical instability. Looking ahead, the practical EP enhancement can be further improved through integrated photonics techniques, such as on-chip optical devices based on silicon nitride, lithium niobate, and III-V active semiconductors. The coupling phase can be finely tuned using high-speed electrical signals, allowing real-time control of the EP states.

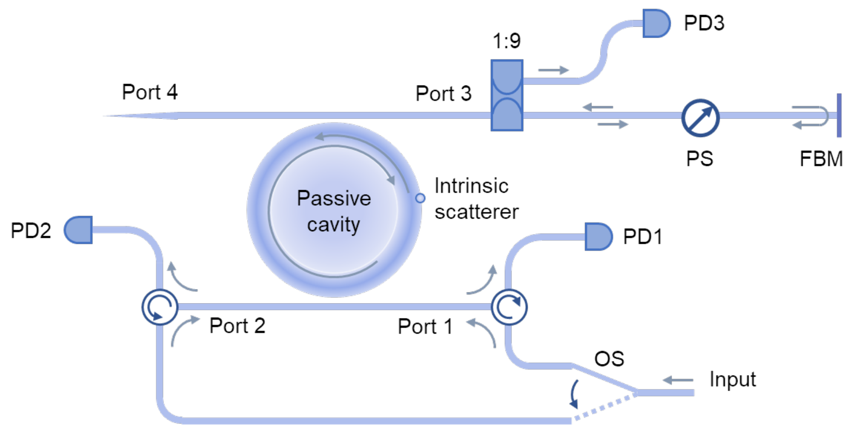

Supplementary Figure 8 | Experimental setup for the chirality measurement. When inputting the CW mode, the transmission spectra are monitored by PD2, and the intensities of CCW and CW modes are measured by PD1 and PD3, respectively. For the CCW input direction, PD1 is used to monitor the transmission spectra, while both PD2 and PD3 measure the intensity of CW modes. PD, photodetector; PS, phase shifter; FBM, fiber-based mirror; OS, optical switch.

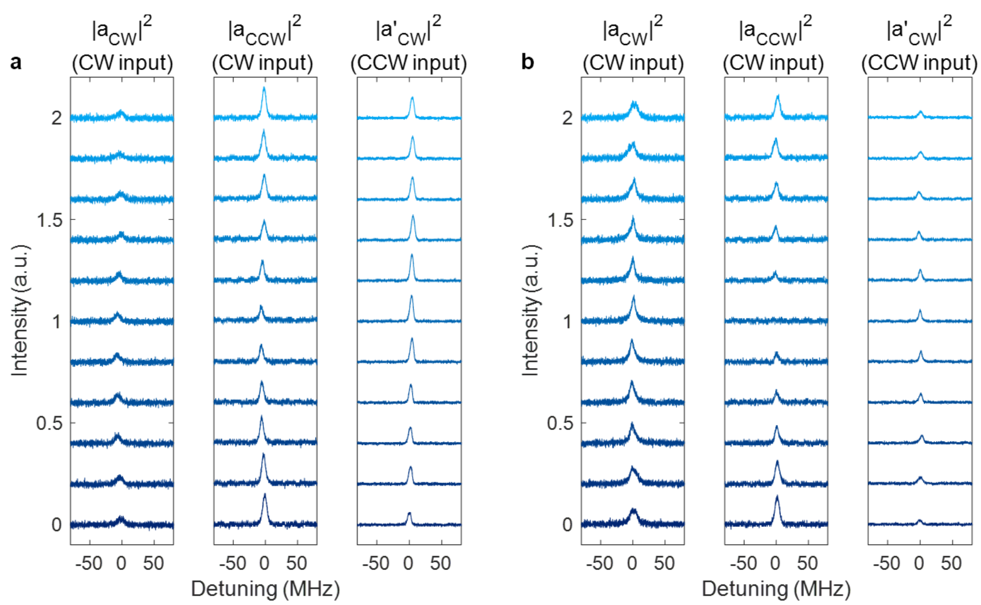

Supplementary Figure 9 | Intensities of CW and CCW modes for different input directions. Vertical axis: varying $\Delta\varphi$ within $[-\pi, \pi]$. **a**, $\mu < A$. **b**, $\mu = A$. The reflection vanishes at the EP with the CW input direction.

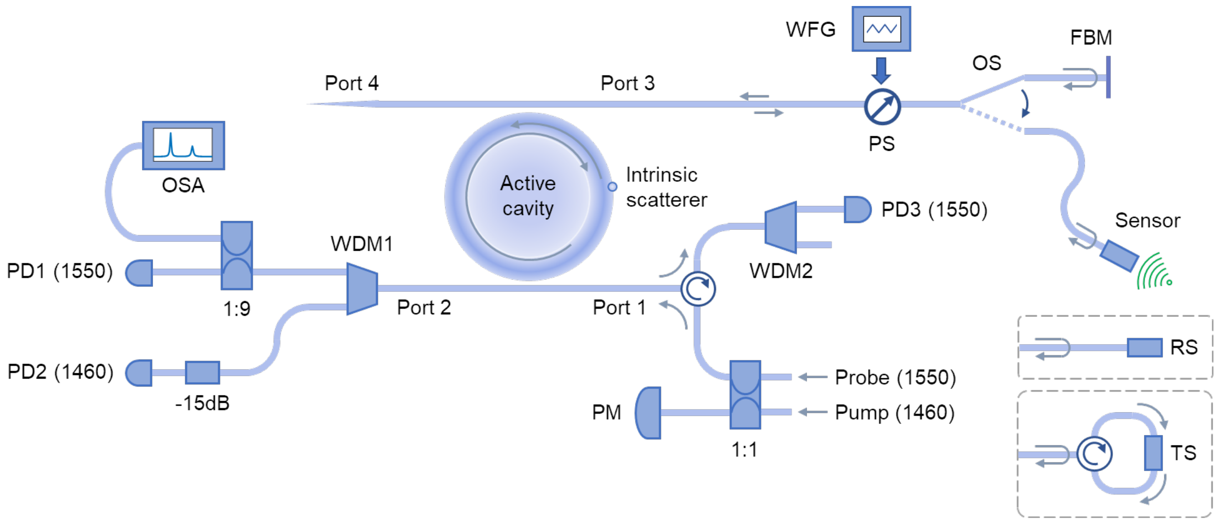

Supplementary Figure 10 | Experimental setup for splitting measurements. The active cavity, pumped by the 1460-band light, provides optical gain for linewidth narrowing in the 1550-band probe light. PD1 and PD2 monitor the transmission spectra of the probe light and the pump light, respectively. The EP states are confirmed by zero reflections at PD3. PS adjusts the phase offset φ_0 for realizing EPs as well as for the compensation of additional frequency-related phase changes (Methods and Supplementary Figure 14). Through the manual OS, the port 3 of the control unit connects to either FBM for the splitting characterization, or to the remote sensor for sensing experiments. WFG, waveform generator; PS, phase shifter; OS, optical switch; FBM, fiber-based mirror; OSA, optical spectrum analyzer; WDM, wavelength-division multiplexing; PD, photodetector; PM, power meter; RS, reflection-type sensor; TS, transmission-type sensor.

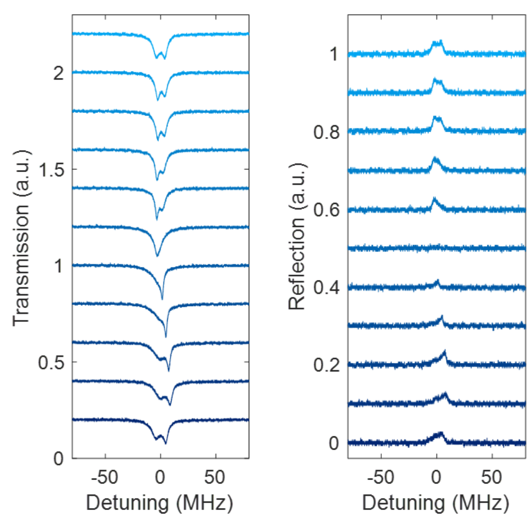

Supplementary Figure 11 | Transmission and reflection spectra while tuning around an EP. From bottom to top, varying $\Delta\varphi$ from $-\pi$ to π. The EP state exhibits an unsplit transmission spectrum and a zero reflection.

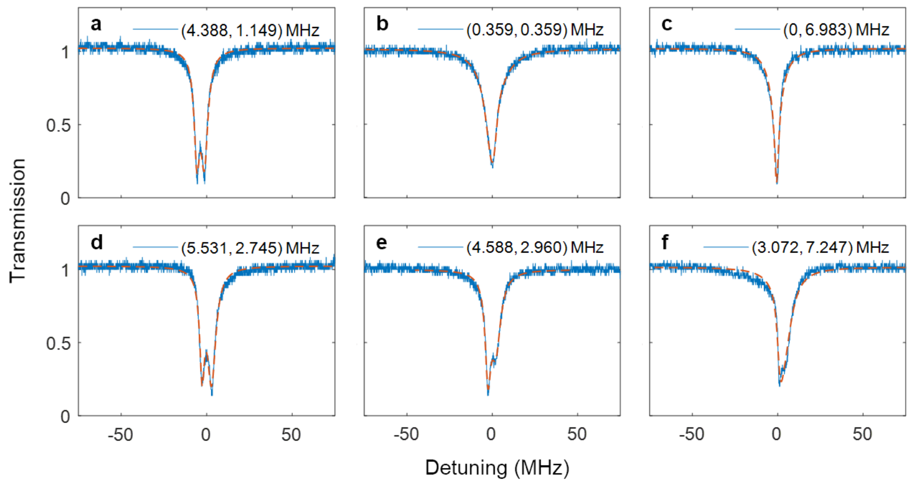

Supplementary Figure 12 | Extraction of splitting from the transmission spectra. The curve fitting is implemented using the expression derived in the Methods section. Legend: (frequency splitting = $|2\Omega/2\pi|$, linewidth difference = $|2\Gamma/2\pi|$).

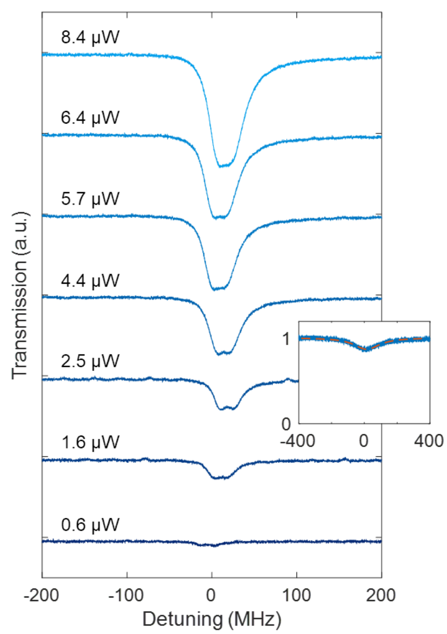

Supplementary Figure 13 | Transmission spectra with increasing probe power. The probe light in the active cavity opens a lossy channel for the gain provided by the pump[4]. Therefore, higher probe power compromises the ability to using optical gain to narrow the linewidth. Inset: Broader Lorentzian lineshape of the probe light without the pump light. Our system works in the under-coupling regime.

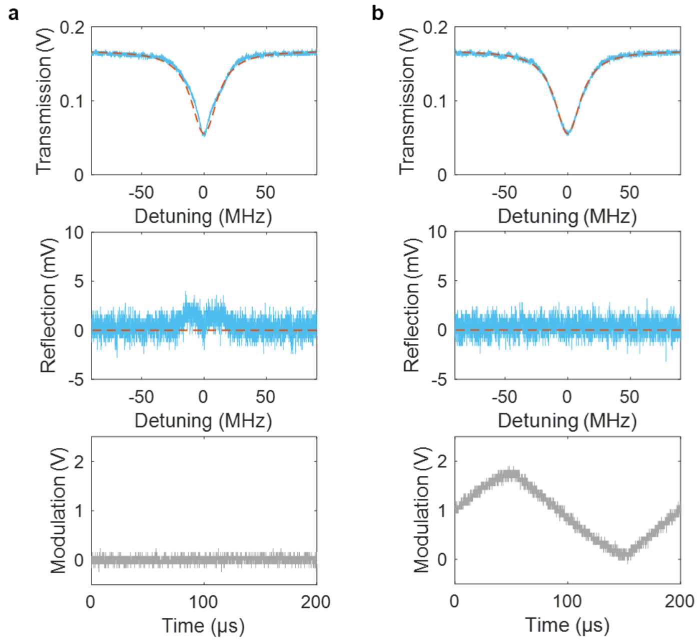

Supplementary Figure 14 | Compensation of additional phase change induced by frequency scanning. a, Without the modulation signal, the EP state is only achieved at zero detuning, which is confirmed by the zero reflection. The non-zero reflection elsewhere indicates the deviation from the EP state, because the frequency detuning leads to additional phase change (Methods). Also, the lineshape also deviates from the theoretical expectation. **b**, With the modulation signal (4.98 kHz), the effect of the frequency-induced phase change is suppressed. The reflection remains zero at different detuning, and the lineshape of the transmission spectrum is recovered.

References

1. Peng, B. *et al.* Loss-induced suppression and revival of lasing. *Science* **346**, 328–332 (2014).

2. Yariv, A. Universal relations for coupling of optical power between microresonators and dielectric waveguides. *Electron. Lett.* **36**, 321–322 (2000).

3. Liang, G. *et al.* Robust, efficient, micrometre-scale phase modulators at visible wavelengths. *Nat. Photonics* **15**, 908–913 (2021).

4. Lei, F., Peng, B., Özdemir, Ş. K., Long, G. L. & Yang, L. Dynamic Fano-like resonances in erbium-doped whispering-gallery-mode microresonators. *Appl. Phys. Lett.* **105**, 101112 (2014).